Title
DWI and DCE-MRI approaches for differentiating reversibly electroporated penumbra from irreversibly electroporated ablation zones in a rabbit liver model.

Journal
American Journal of Cancer Research, 9(9)

ISSN
2156-6976

Authors
Shangguan, Anna J
Sun, Chong
Wang, Bin
et al.

Publication Date
2019

Peer reviewed

Am J Cancer Res 2019;9(9):1982-1994
www.ajcr.us /ISSN:2156-6976/ajcr0100422

Original Article

DWI and DCE-MRI approaches for differentiating reversibly electroporated penumbra from irreversibly electroporated ablation zones in a rabbit liver model

Anna J Shangguan[1,2*], Chong Sun[1,3*], Bin Wang[1,4], Liang Pan[1,5], Quanhong Ma[1], Su Hu[1,6], Jia Yang[1], Aydin Eresen[1], Yuri Velichko[1], Vahid Yaghmai[1], Zhuoli Zhang[1]

[1]Department of Radiology, Feinberg School of Medicine, Northwestern University, Chicago, IL, USA; [2]Medical Student Training Program, Northwestern University, Chicago, IL, USA; [3]Department of Orthopaedics, The Affiliated Hospital of Qingdao University, Qingdao, Shandong, China; [4]Department of Hepatobiliary and Pancreatic Surgery, The Second Affiliated Hospital, Zhejiang University School of Medicine, Hangzhou 310009, China; [5]Department of Radiology, The Third Affiliated Hospital of Suzhou University, Changzhou, Jiangsu, China; [6]Department of Radiology, The First Affiliated Hospital of Soochow University, Suzhou, Jiangsu, China. [*]Co-first authors.

Received August 1, 2019; Accepted August 13, 2019; Epub September 1, 2019; Published September 15, 2019

Abstract: The purpose of our study was to investigate the hypothesis that DWI-MRI and DCE-MRI cab be used to distinguish between IRE and RE zones of IRE treatment in a rabbit liver model. 6 rabbits underwent baseline and post-procedure MR imaging with DWI and DCE-MRI as well as IRE (10 pulses, 2000 V, 10 μs/pulse, 10 ms between pulses). Rabbits were euthanized immediately after post-procedure MRI to acquire liver tissue for histology. Liver tissues were fixed and then stained with HE and TUNEL. T1w and T2w intensities in different treatment zones were calculated and normalized to paraspinal muscle signal. ADC maps were generated from DWI. AUC, PE, TTP, WIS, Ktrans, Kep, and V_E were calculated from DCE-MRI. Apoptosis index was calculated from TUNEL stained tissues. $P<0.05$ was considered statistically significant. Entire IRE treated region was hyperintense compared with untreated tissues on T1w, with the RE zone having a higher signal intensity. On DWI, IRE treated tissue had decreased ΔADC. The IRE zone has a lower ΔADC than the RE zone within the treated region. On DCE-MRI, IRE zone demonstrated the highest TTP and the lowest PE, WIS, Ktrans, Kep, and V_E, followed by the RE zone then the untreated tissue. TUNEL staining of liver tissues showed that the IRE zone had the highest apoptosis index, followed by the RE zone and then untreated tissue. In conclusion, DCE-MRI and DWI parameters allow differentiation between RE and IRE zones in a rabbit liver model.

Keywords: DCE-MRI, IRE, HCC, MRI, perfusion

Introduction

Irreversible electroporation (IRE) is a novel class of locoregional tissue ablation that involves delivery of electrical pulses to targeted tissues, leading to formation of nanometer-scale pores in the cell membrane [1-3]. In central regions of irreversible ablation, the nanopores are permanent, leading to cell death and tissue necrosis (defined as irreversibly electroporated zone, IRE zone) [4, 5]. In the peripheral reversibly electroporated penumbra (defined as reversibly electroporated zone, RE zone), the nanopores are transient and closes within minutes after IRE, leading to only some reversible tissue alterations. The sizes of the IRE and RE zones depend on a variety of factors, including the applied voltage, number of pulses, and duration of pulses [5-7]. Compared with other loco-regional ablation techniques, IRE generates clear margins between treated and untreated tissues and does not undertreat targeted tissues [2, 5]. Unlike other thermal techniques, IRE also protects surrounding healthy tissue from thermal tissue damage and the heat sink effect. Furthermore, the high collagen content of blood vessel (BV) extracellular matrix (ECM) protects the RE zone blood vessels from damage and cell death, thus potentially mitigating side effects such as hemorrhage and tissue hypoxia [2, 8, 9].

Most interestingly, previous studies have shown that IRE treatment area can be visualized by imaging techniques immediately after IRE, allowing for potential peri-operative monitoring of treatment [10, 11]. Magnetic resonance (MR) imaging is a particularly attractive method for visualizing treatment margins as it offers superior soft tissue contrast compared with other imaging methods, is not affected by issues of tissue penetrance, and does not expose patients to ionizing radiation [5, 11-13]. More importantly, MRI has previously been used to visualize and quantify tissue changes after electroshock trauma in muscle tissues, demonstrating its potential for monitoring tissue changes after IRE [14]. Previous publications also showed that common sequences such as T1 FLASH, contrast enhanced inverse recovery, and T2 can be used to visualize liver tumor treatment margins in IRE in rat and rabbit models [5]. However, previous studies have focused only on the correlation between imaging findings and IRE ablation to allow discrimination between tumor and normal tissue regions and did not study MRI prediction of the margins between IRE and RE zones. This is significant as incomplete tumor treatment in the RE zone leads to risk of tumor recurrence or progression, limiting its widespread clinical application.

Diffusion weighted imaging (DWI) specifically probes the Browning motion of water molecules through imaged tissues [15]. Apparent diffusion coefficient (ADC) is a quantitative MRI measurement calculated from DWI that correlates with structural properties of the imaged tissue as well as cell apoptosis within tissues [16-18]. Clinically, dynamic contrast enhanced MRI (DCE-MRI) is used for visualization of tissue perfusion, vascular blood flow, blood vessel permeability, and tissue contrast uptake [19, 20]. Quantitative MRI measurements such as area under curve (AUC), the transfer constant k_{trans}, and flux rate constant k_{ep}, can be calculated from DCE-MRI using various pharmacokinetic models to quantitatively evaluate tissue changes after IRE treatment [21, 22].

The purpose of our study was to investigate the hypothesis that DWI MRI and DCE-MRI cab be used to distinguish between IRE and RE zones of IRE treatment in a rabbit liver model.

Materials and methods

General experimental methods

IRE was performed on normal liver parenchyma. Each animal underwent the IRE procedure as well as baseline and 30 min post-procedure imaging with T1 weighted (T1w), T2w weighted (T2w), DWI, and DCE-MRI sequences. All animals were euthanized immediately after post-IRE image acquisition. Both treated and untreated liver tissues were collected for histology.

Animal model

All experiments were approved by the institutional animal care and use committee of Northwestern University. 6 New Zealand white rabbits (Covance, Princeton, NJ, USA) underwent IRE at 2000 V as well as baseline and post-procedural MR imaging. Anesthesia was induced by intramuscular injection of ketamine (100 mg/kg, Fort Dodge Animal Health, Fort Dodge, IA) and xylazine (5 mg/kg; Abbott Laboratories, North Chicago, IL). Ventilation with isoflurane (2-3% with 100% oxygen, 3 L/min, Patterson Veterinary, Greeley, CO) via breathing mask was used for anesthesia maintenance throughout imaging and IRE procedure. An ear vein catheter was inserted prior to baseline image acquisition for IV delivery of Gd-DTPA (Magnevist®; Berlex, Montville, NJ, U.S.A) for DCE-MRI. All animals were euthanized immediately after post-procedural scans to obtain liver samples for histology.

IRE procedure

The left median lobe of the liver was exposed by median laparotomy. Two paralleled MRI-compatible needle electrodes with 1-cm spacing (platinum-iridium materials; Microprobes, Gaithersburg, MD) were inserted into the center of the left median lobe to a 1-cm depth. Electrode separation was maintained by securing the needles in a 15-mm-thick plastic spacing block. Next, the electrodes were connected to the IRE generator (ECM830; Harvard Apparatus, Holliston, Mass) to apply 2000-V square wave pulses (number of pulses, 10; each pulse duration, 100 μs; interval between pulses, 100 ms) [5, 10]. The IRE procedure was performed over 10 minutes by two authors (B.W. and C.S., both with 2 years of experience).

Table 1. Summary of MRI acquisition parameters

	Sequence	Acquisition plane	TR (msec)	TE (msec)	FOV (mm^2)	FA	Voxel size (mm^3)
T2WI	SE	Coronal	1660.0	39	180×180	150	0.5×0.5×2.0
T1WI	GR	Axial	200	2.93	180×180	70	0.8×0.8×2.0
T2WI	SE	Axial	1660.0	39	180×180	150	0.5×0.5×2.0
DWI	EP	Axial	1300	65	153×124	90	0.8×0.8×2.0
DCE-MRI	GRE	Axial	3771	39	180×180	150	0.47×0.47×2.0

Twenty minutes after IRE, rabbits were transferred to the adjacent MRI suite for additional imaging.

General MR imaging methods

All images were acquired using a knee coil (Tx/Rx 15-Channel Knee Coil; Siemens Medical Solutions, Erlangen, Germany) in a 3.0-T clinical MR imaging unit (Magnetom Skyra; Siemens Medical Solutions, Erlangen, Germany), with the animal in a prone position. T1w, T2w, and DWI were acquired immediately before and after the IRE procedure. Acquisition parameters are summarized in **Table 1**.

Imaging analysis

All anatomic images were analyzed using the open-source software ITK-SNAP (version 3.6, University of Pennsylvania). Regions of interest were drawn around both IRE and RE zones of IRE treatment as well as in untreated tissues and para-spinal muscles for normalization. ADC maps were generated by post-processing of diffusion-weighted images using MatLab R2016b (Mathworks, Natick, MA). A freehand ROI Change in signal was measured as $signal_{PostIRE} - signal_{Baseline}$. Normalized $\Delta T1_{signal}$ is calculated as $\triangle T1_{Normalized} = \frac{T1_{treated} - T1_{untreated}}{T1_{paraspinal\ muscle}}$, where $T1_{treated}$ is T1 of IRE treated tissue, $T1_{untreated}$ is T1 of untreated tissue, and $T1_{paraspinal\ muscle}$ is T1 of the paraspinal muscles. ΔADC is calculated as $\Delta ADC = ADC_{treated\ tissue} - ADC_{normal\ tissue}$.

DCE-MRI methods

DCE-MRI was performed immediately after acquisition of T1w, T2w, and diffusion images to prevent imaging artifacts from pressure injection of contrast at both baseline and post-IRE image acquisition. Images of the targeted sections were acquired every 2.6 s. During image acquisition, baseline DCE-MRI images were acquired for 60 s. After initial image acquisition, 8 μL/g Gd-DTPA solution (Magnevist®; Berlex, Montville, NJ, U.S.A) was delivered over 10 s via an ear-vein catheter, followed by flushing with bolus 5 mL saline through the same ear vein catheter. An additional set of T1w images was acquired immediately after DCE-MRI. Imaging parameters are also summarized in **Table 1**.

DCE-MRI analysis

All DCE-MRI images were initially post-processed using Jim7 (Xinapse Systems Ltd., West Bergholt, Essex, UK). ROIs were drawn around the IRE and RE zones of IRE treatment as well as around untreated liver tissue, with anatomic T1w and T2w images as reference. Time-intensity curves (TICs) were generated for each ROI, and the following semi-quantitative parameters were generated: peak enhancement (PE, the maximal signal intensity minus baseline signal intensity), time to peak (TTP, the time from the initiation of enhancement to PE), wash-in slope (WIS, the maximal upslope reaching PE), and the areas under the curve over 30, 60, 90, 120, 150 and 180 seconds (AUC_{30}, AUC_{60}, AUC_{90}, AUC_{120}, AUC_{150} and AUC_{180}) after the initiation of enhancement. Quantitative measurements of DCE-MR images was performed using Platform for Research in Medical Imaging (PMI, University of leeds, Leeds, United Kingdom). A dual-inlet 2-compartment modified Tofts model that accounts for contrast arrival from both the hepatic artery and main portal vein was used to calculate the following quantitative measurements: K_{trans} (volume transfer constant from the plasma to the extra-vascular extra-cellular space (EES)), K_{ep} (flux constant), and V_e (the EES volume fraction). ROIs drawn from TIC analysis was transferred to maps of the quantitative measurements.

Histologic analysis

After post-IRE image acquisition, all animals were euthanized. Both IRE-treated tissues and

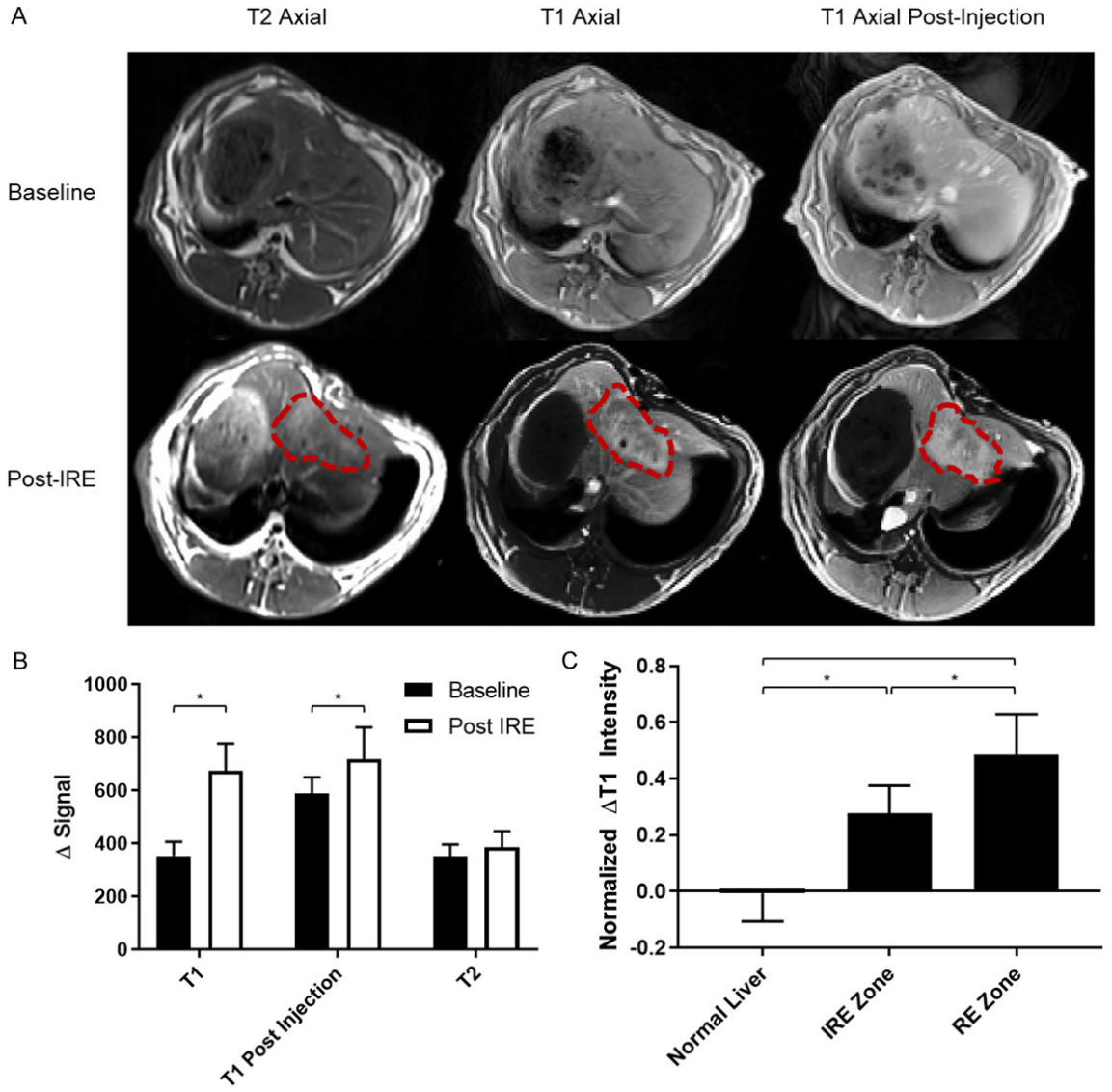

Figure 1. Anatomic MR images and analysis. A. Representative MR images before and after IRE ablation. Pre- and post-contrast T1w images as well as T2w images are shown. IRE treatment margins are traced by red dashed lines. B. Changes in signal intensity averaged across entire IRE-treated region. Signal was normalized to paraspinal muscle intensity, which are similar across all images. *Represents significant differences in Δintensity before and after IRE treatment ($P<0.005$). Statistical difference was assessed by t-test. C. Changes in pre-contrast T1w intensity in untreated tisues and Ire treatment zone. Zignal intensity is normalized to paraspinal muscle intensity. Differences in signal intensity was assessed by one-way ANOVA. *Represents significance ($P<0.05$).

untreated liver tissues were fixed in formalin immediately after euthanasia and later stained with hematoxylin-eosin (HE) stain, terminal deoxynucleotidyl transferase dUTP nick end labeling (TUNEL) stain, and anti-CD34 stain to target endothelials cells in liver tissues. All images were examined using ImageJ. Tumor tissue apoptosis was identified on TUNEL-stained slices and quantified as the percentage of TUNEL-positive cells/total cells in 3 representative fields at 400× magnification randomly selected from each slice.

Statistical analysis

All statistical analyses were performed using GraphPad Prism (GraphPad Software, La Jolla, CA). The results are presented as mean ± standard deviation (SD). Differences in DCE-MRI parameters and hepatocyte apoptosis among

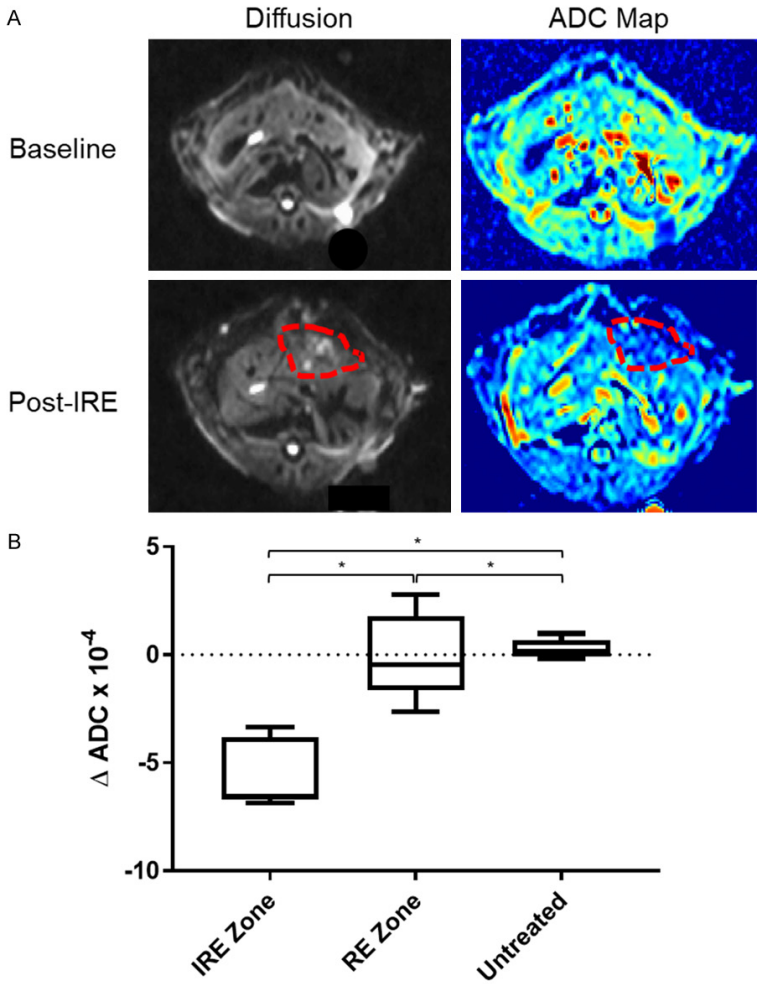

Figure 2. Diffusion weighted images and analysis. A. Representative DWI and ADC maps before and after IRE treatment. Red-dashed lines enclose margins of IRE treatment. B. Changes in ADC before and after IRE treatment for untreated tissues, IRE zones, and RE zones. One-way ANOVA showed that untreated tissues, IRE zone, and RE zone had significantly different ΔADCs after IRE (*, P<0.05).

the normal liver parenchyma, the RE and IRE zones were determined by the Kruskal-Wallis test followed by pairwise comparisons. The relationship between DCE-MRI parameters and hepatocyte apoptosis was assessed by Pearson correlation coefficients (r). P<0.05 was considered to indicate a significant difference in all statistical tests.

Results

Anatomic MR imaging

Representative axial T1w and T2w images before and after IRE are presented in **Figure 1A**. After IRE, an ovaloid ablated region with heterogeneous intensity that is perpendicular to direction of probe insertion can be clearly delineated from surrounding untreated tissues. On both T1w and T2w images, the treatment region contained a hypointense central zone that correlated with IRE zone surrounded by a hyperintense peripheral zone that correlated with RE zone. The IRE treatment region was clearly delineated from the surrounding untreated tissue on both T1w and T2w images. The IRE and RE zones with the treatment region could be clearly delineated from each other on only T1w images.

After normalization, ROIs were drawn around the entire IRE-treated region as well as around the IRE and RE zones within the treated region for quantification of signal intensity. The entire treated region demonstrated higher signal intensity (P<0.05) compared with untreated tissues on both T1w and T2w images (**Figure 1B**). On T1w images, both IRE and RE zones demonstrated an increase in intensity (P< 0.05) compared with untreated tissues; the RE zone had a greater intensity and increase in intensity (P<0.05) than the IRE zone on T1w images (**Figure 1C**). Both T1w and T2w sequences allowed differentiation of treated from untreated tissues. T1w images further allowed differentiation of IRE and RE ablation zones within the treatment region.

Diffusion weighted imaging of normal rabbit liver over IRE ablation

Figure 2A shows representative pre- and post-IRE axial diffusion weight images and ADC maps. Like in T1w and T2w images, treatment regions on DWI and ADC maps are delineated from surrounding untreated tissue and displayed heterogeneous intensity. The IRE and RE zones within the treatment regions can be

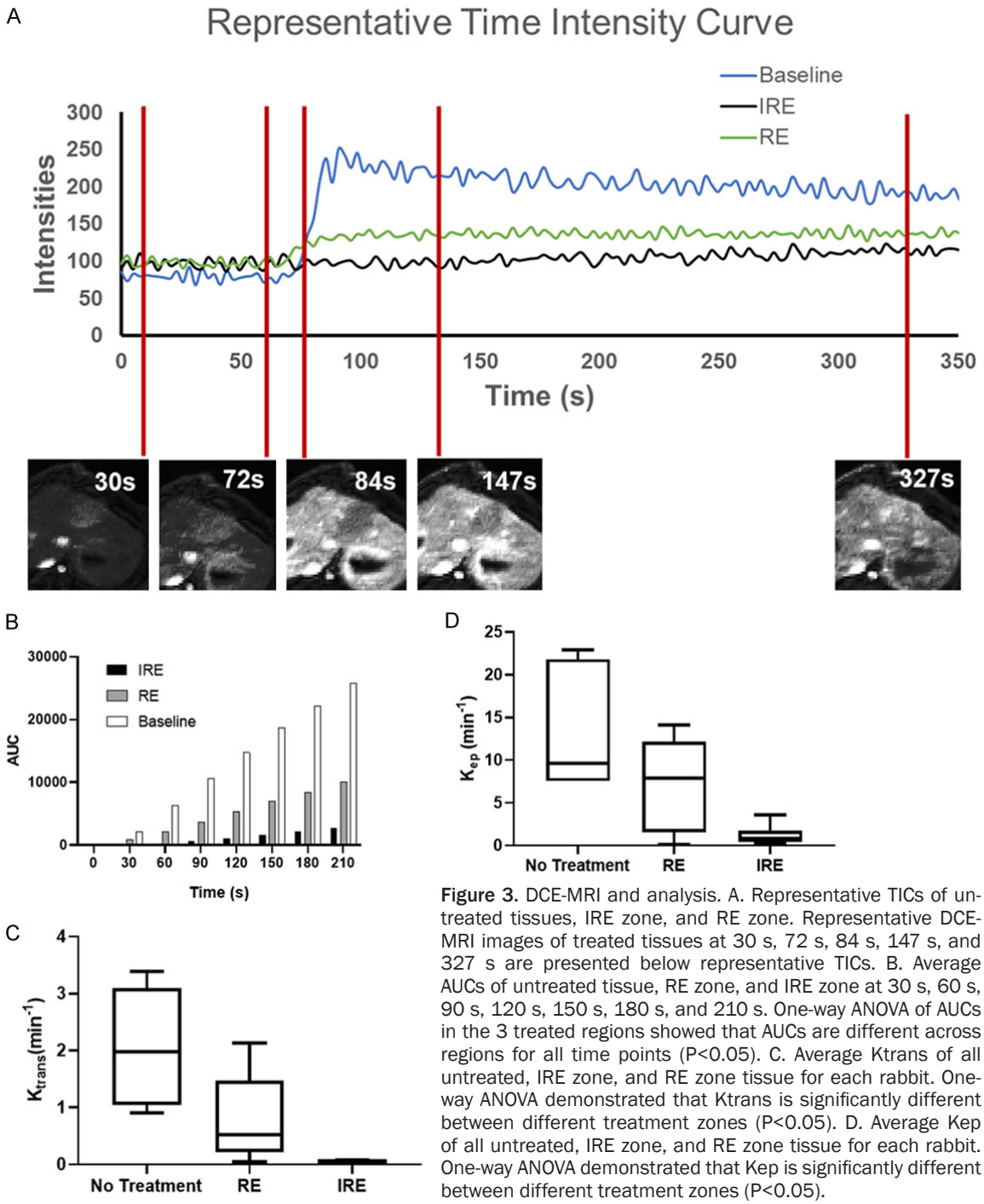

Figure 3. DCE-MRI and analysis. A. Representative TICs of untreated tissues, IRE zone, and RE zone. Representative DCE-MRI images of treated tissues at 30 s, 72 s, 84 s, 147 s, and 327 s are presented below representative TICs. B. Average AUCs of untreated tissue, RE zone, and IRE zone at 30 s, 60 s, 90 s, 120 s, 150 s, 180 s, and 210 s. One-way ANOVA of AUCs in the 3 treated regions showed that AUCs are different across regions for all time points ($P<0.05$). C. Average Ktrans of all untreated, IRE zone, and RE zone tissue for each rabbit. One-way ANOVA demonstrated that Ktrans is significantly different between different treatment zones ($P<0.05$). D. Average Kep of all untreated, IRE zone, and RE zone tissue for each rabbit. One-way ANOVA demonstrated that Kep is significantly different between different treatment zones ($P<0.05$).

differentiated from each other on ADC maps. ΔADC is the difference between ADCs of zones in the treatment region and that of untreated tissues. The IRE zone in the treatment region showed a decreased ΔADC ($P<0.05$) compared with untreated tissues and the RE zone in treatment zones, which did not significantly differ from each other (**Figure 2B**).

DCE-MRI of IRE treatment

DCE-MRI is the last set of images acquired prior to IRE ablation or animal euthanasia to prevent contrast-related artifacts on other MR sequences. **Figure 3A** representative time intensity curve (TIC) of untreated liver tissue and RE and IRE zones of treated tissues over the duration

Table 2. Summary of semiquantitative and quantitative analysis of DCE-MRI

Parameter	Normal Liver	RE Zone	IRE Zone
AUC_{30}	2158±945.7	380.0±644.2	55.83±131.0
AUC_{60}	6334±1289	2111±1402	239.0±393.3
AUC_{90}	1.065×10^5±1647	3680±2234	598.5±738.1
AUC_{120}	1.472×10^5±2049	5324±3094	1055±1134
AUC_{150}	1.864×10^5±2447	6952±3966	1573±1586
AUC_{180}	2.209×10^5±2837	8449±4747	2103±2020
TTP	27.67±6.907	67.7±21.8	298.7±114.1
PE	183.9±42.31	59.93±36.15	47.63±31.64
WIS	6.847±1.504	1.008±0.7557	0.1877±0.1633
K_{trans}	206.0±102.1	79.12±76.89	4.049±1.767
K_{ep}	1313±716.0	1077±1040	121.3±119.7
V_e (%)	18.54±4.510	11.18±6.579	5.695±2.768

of DCE-MRI data acquisition with corresponding images at pre-contrast-injection, initial contrast arrival, contrast plateau, and end of image acquisition. All tissues demonstrated low signal intensity at the beginning of data acquisition until contrast arrival around 1 min after start of image acquisition. At contrast arrival, untreated liver tissue demonstrated the greatest and earliest increase in tissue signal intensity leading to signal peaking and then plateau at a level slightly below signal peak. The RE zone TIC showed a slow increase of tissue signal after contrast arrival leading to signal plateau at around maximum signal intensity. The IRE zone showed little to no change in tissue contrast over duration of image acquisition. At all time points, the treatment zone was clearly delineated from the untreated tissues, and different ablation zones within the treated tissue can be differentiated from each other. Area under TIC is normalized to baseline signal, and area under the curve (AUC) was calculated every 30 s and averaged across all animals (**Figure 3B** and **Table 2**). Similar to visual observation in **Figure 3A**, untreated regions demonstrated greatest increase in intensity compared with both RE and IRE zones. Within the treated tissue, the RE zone demonstrated a slight increase in total intensity over time, while IRE zone showed almost no increase in intensity over time.

Semiquantitative analysis was performed on TICs, and the following parameters were generated (**Table 2**): time to peak (TTP, the time from contrast arrival to time at peak contrast), peak enhancement (PE, the difference between baseline tissue contrast and peak tissue contrast), and wash-in slope (WIS, the rate at which tissue intensities increase from baseline to peak signal intensity). Among examined regions, the IRE zone in the treated region demonstrated the longest TTP (298.68±114.18 s), followed by the RE zone (67.7±21.81 s) and untreated tissue (27.7±6.91 s, $P<0.05$). In contrast, IRE zone demonstrated the least PE (46.62±31.64), followed by RE zone (59.92±36.14) and untreated tissues (183.89±42.31, $P<0.05$). The longer TTP in the IRE and RE zones suggested that the treated region had a slower rate of contrast distribution. Moreover, the lower PE within the treated region also suggested that the treated region had a lower contrast concentration than untreated regions. Notably, as WIS for the IRE zone was nearly zero, almost no vascular contrast distribution, and thus perfusion, was present in the IRE zone. The low but nonzero WIS in the RE zone suggested that contrast arrival and distribution were present but delayed and diminished, respectively.

Quantitative analysis of DCE-MRI images was performed using a dual-input 2-compartment modified Tofts pharmacokinetics model. The following parameters were calculated and summarized in **Table 2**: K_{trans} (volume transfer coefficient that represents vascular permeability), K_{ep} (flux rate constant), and V_e (extravascular extracellular volume). The untreated tissue had the greatest K_{trans} (206.0±102.1), followed by the RE zone (79.12±76.89) and the IRE zone (4.049±1.767, $P<0.05$). Similarly, the untreated tissue had the greatest K_{ep} (1313±716.0), followed by the RE zone (1077±1040) and the IRE zone (121.3±119.7, $P<0.05$). The untreated tissue also had the greatest V_e (18.54±4.510), followed by the RE (11.18±6.579) and IRE (5.695±2.768, $P<0.05$) zones. All indicated of a low perfusion of contrast into the treated tissue and slow distribution of contrast within the treated tissue (IRE more so than RE zones), consistent with results of semiquantitative analysis.

Histologic analysis

Figure 4 shows representative histology of IRE zone, RE zone, and untreated tissues stained

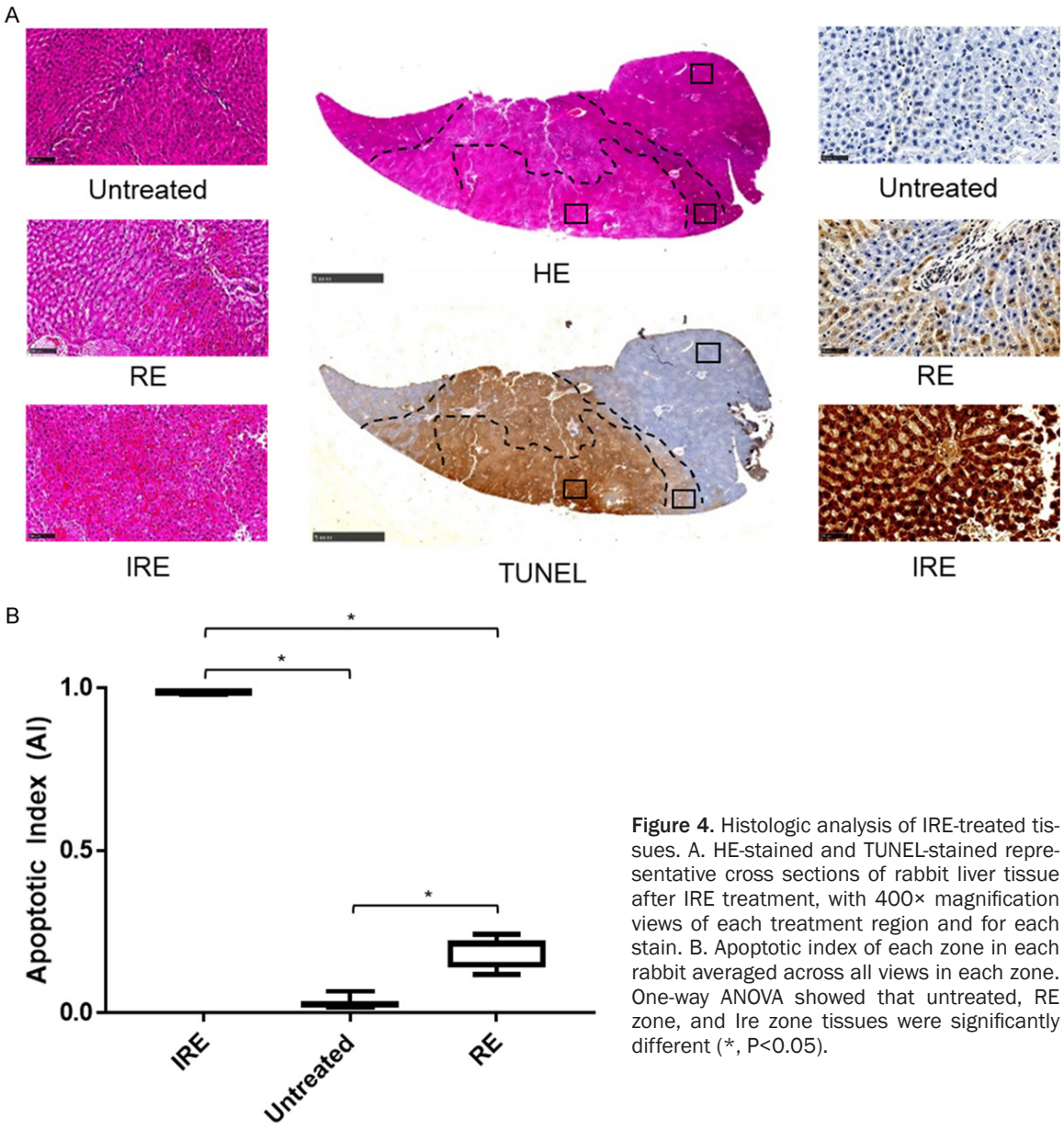

Figure 4. Histologic analysis of IRE-treated tissues. A. HE-stained and TUNEL-stained representative cross sections of rabbit liver tissue after IRE treatment, with 400× magnification views of each treatment region and for each stain. B. Apoptotic index of each zone in each rabbit averaged across all views in each zone. One-way ANOVA showed that untreated, RE zone, and Ire zone tissues were significantly different (*, $P<0.05$).

for HE and TUNEL. On both HE and TUNEL stains, the IRE treated regions were demarcated from untreated tissue with clear margins (**Figure 4A**, **4B**). Margins between RE and IRE zones were clear on HE images, but less clear on TUNEL-stained sections. As tissue used for HE and TUNEL staining were sliced sequentially at <10 μm per slice, treatment zone margins drawn on HE stained sections could be easily applied to TUNEL stained sections, as seen in **Figure 4A**, **4B**.

Untreated tissue, RE zone, and IRE zone had different histologic appearances on HE stained sections. Untreated tissues showed normal liver tissue structure, where hepatocytes form liver sinusoids with few red blood cells (RBCs) within liver sinusoids. In contrast, centrally located IRE-zone demonstrated coagulative tissue necrosis along with massive RBC congestion in liver sinusoids, destruction of liver parenchymal structure, and blurring of hepatocyte cell membrane from apoptosis. In peripherally located RE zone, liver tissue demonstrated mild RBC congestion in the liver sinusoids with tissue hyperemia, hepatocyte swelling, and overall preserved liver parenchymal structure.

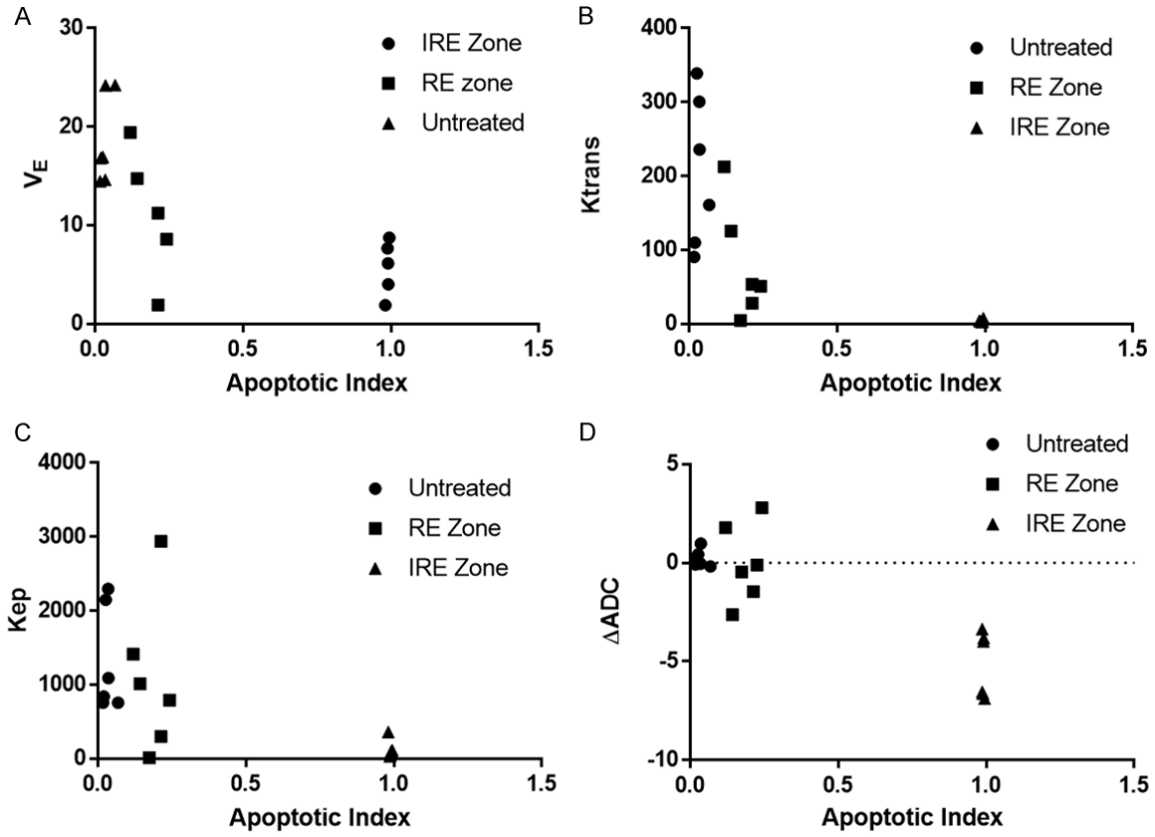

Figure 5. Comparisons of MRI measurements and apoptotic index. Average V_E (A), Ktrans (B), Kep (C), or ADC (D) vs apoptotic index for each untreated tissue, RE zone, and IRE zone in each rabbit. V_E, Ktrans, Kep, or ADC were averaged across the entire region. AI is averaged across all histology views at 400× magnification.

In TUNEL stained sections, the IRE treated region overall stained strongly positive for apoptosis (**Figure 4A**). While distinct RE and IRE zones could be visualized by differences in staining intensity, no clear margins could be visualized between the 2 zones (zone margins were taken from margins seen on HE sections). IRE zone showed massive cell death, with almost all cells staining strongly and positively on TUNEL (apoptosis index = 0.988±0.00426. RE zone showed a mix of cells staining positively and negatively on TUNEL (apoptosis index = 0.190±0.0459). The untreated region stained mostly negatively on TUNEL with a few cells staining positively per field at 400× magnification (apoptosis index = 0.0311±0.0180). This was expected given that IRE can generate clear treatment margins without damaging adjacent tissue. One-way ANOVA of TUNEL staining in the RE zone, IRE zone, and untreated tissue demonstrated significant difference between the 3 regions (**Figure 4B**, $P<0.05$), with IRE zone having the greatest apoptosis, followed by the RE zone and then the untreated tissue.

Tissue apoptosis was compared with quantitative DWI and DCE-MRI measurements, including ΔADC, K_{ep}, K_{trans}, V_E, PE, TTP, and WIS (**Figure 5**). For all comparisons, the 3 regions of comparison showed distinct separation and clustering. Due to high apoptosis in the IRE zone, the IRE group generally clustered closely together, but all 3 regions were clearly distinguishable from each other for all comparisons. No correlations were found between imaging measurements and apoptotic index ($P > 0.05$).

Discussion

IRE is a potentially powerful tool that allows treatment of liver tumors with minimal adverse effects. It generates different zones of ablation with different treatment efficacies that are hard to visualize on normal imaging immediately after IRE, limiting peri-treatment monitoring

and prediction of treatment response. Although BVs in IRE-treated tissues may potentially be shielded from electrical damage by the high collagen content in BV ECM, functional changes of blood vessel integrity and general tissue perfusion post-IRE has not been investigated. In this project, we demonstrated that DWI and DCE-MRI both allow visualization of margins between IRE and RE zones. Both semi-quantitative (PE, TTP, WIS) and quantitative (K_{trans}, K_{ep}, V_E) DCE-MRI measurements allow distinguishing RE and IRE zones from each other. The semi-quantitative and quantitative DCE-MRI measurements also showed that the IRE zone had no perfusion after IRE, while the RE zone had partially preserved tissue perfusion. Histology confirmed that IRE zone had complete tissue death with destruction of tissue architecture, while RE zone had partial some tissue death and preservation of tissue architecture.

Ablative therapies such as radiofrequency ablation and cryoablation are a key class of treatment in liver cancer and is FDA-approved for cure of early stage cancer along with surgical resection as well as treatment of advanced disease [23]. However, these thermal ablative therapies suffer from severe side effects including hemorrhage and destruction of healthy adjacent tissue. In contrast, electrical ablative therapies such as IRE deliver electrical pulses that generate clear treatment margins and do not damage adjacent healthy tissue [24-27]. As a result, IRE causes only mild side effects such as local pain, nausea/vomiting, and transient ascites with no elevated liver enzymes. IRE generates nanopores on hepatocyte membranes that are irreversible in the IRE zone and transient in the RE zone. These transient nanopores in the RE zone provide a unique opportunity for delivery of large quantities of adjuvant therapeutic agents such as multikinase inhibitors and DNA-targeting agents for maximizing cancer treatment efficacy. As thermal techniques damage treatment region BVs and as high collagen ECM of BVs resist IRE electrical damage, assessment of tissue perfusion immediately after IRE may be critical for confirming RE zone margins and thus effective distribution of adjuvant therapies. So far, IRE has been approved for treatment of Stage I and II tumors as well as unresectable disease [28]. In vivo assessment of liver perfusion soon after IRE has not been studied and is necessary should IRE be considered for combination with other chemo- or radiotherapy agents.

It is known that IRE generates 2 distinct zones within the treated region that are distinguishable on histology. Here, we demonstrated that DCE-MRI measurements allow differentiation of these 2 treatment zones. These treatment zones can also be visualized on DCE-MRI, which allowed assessment of normal liver perfusion after IRE by DCE-MRI. Both parametric and non-parametric approaches were used to for assessment of perfusion. Non-parametric semiquantitative analysis empirically characterizes TICs of various regions of the liver and can be easily and rapidly performed without the application of pharmacokinetic models. Although non-parametric analysis has limited correlation with direct physiologic phenomenon such as vascular permeability and blood flow, this type of analysis is easy and fast to apply and more importantly, has some correlations with clinical markers [21]. In our studies, we chose the semiquantitative measurements AUC, PE, TTP, and WIS as they are more strongly related with organ function. The low WIS and AUC, high TTP, and near-zero PE in the IRE zone as seen in our findings demonstrated a near-zero perfusion in the IRE zone likely due to tissue coagulative necrosis and destruction after IRE as was seen on histology studies. In comparison to the IRE zone, the RE zone had a lower TTP and higher WIS, AUC, and PE that are still higher and lower, respectively, than values in the untreated tissue. The delayed peak and diminished enhancement altogether suggest that tissue in the RE zone retained some tissue perfusion that is diminished compared with normal tissue. This finding is consistent with the histology finding of tissue edema and increased RBC in liver sinusoids, which will impede liver sinusoidal blood flow and perfusion. Scatterplot of nonparametric and parametric findings demonstrated distinct clustering for each tissue region, suggesting that semiquantitative measurements may also effectively reflect differences in tissue perfusion and allow differentiation of treatment zones within the treated region.

Quantitative analysis involves generation of an arterial input function (AIF) of changes in tissue contrast over time and fitting the AIF via pharmacokinetic model to calculate coefficients

representing physiologic parameters including K_{trans}, K_{ep}, V_E, and mean transit time. In this project, we used a dual input 2 compartment extended Tofts model (2CXM). The dual-input was necessary as the liver uniquely has 2 sources of arterial input: the hepatic artery branching off of the abdominal aorta and the hepatic portal vein returning from the gastrointestinal tract. 2CXM was chosen as it is a close pharmacokinetic model of liver tissue vasculature that accounts for both the vascular and the interstitial spaces present in the liver tissue. Dual input 2CXM is also a close physiologic model of liver cancer. Several quantitative measurements were examined in our study: K_{trans}, K_{ep}, and V_E. K_{trans} is a measurement of capillary permeability with different physiologic interpretations depending on vascular permeability [21, 29-33]. For tissue with high vascular permeability such as the liver, K_{trans} is a measurement of blood flow as flux across the endothelium is high and thus depends on blood flow through the endothelium. V_E represents the extravascular extracellular space (EES). K_{ep} is calculated by dividing the K_{trans} by V_E. Our studies found that IRE and RE zones showed diminished K_{trans}, K_{ep}, and V_E compared with untreated tissues, with RE zone having greater volumes for all 3 quantitative measurements than the IRE zone. Low V_E in the IRE and RE zones reflect tissue structure damage after IRE ablation found on histology, with IRE zone demonstrating worse tissue damage than the RE zone. Diminished K_{trans} in the IRE and RE zones reflect decreased blood flow to both regions, with IRE zone having worse blood flow. This diminished blood flow is consistent with histology studies demonstrating tissue coagulative necrosis and RBC congestion in both IRE and RE zones, respectively. Interestingly, K_{ep} remains similar between RE zone and untreated tissues while that in the IRE zone is greatly diminished, suggesting a similar rate of transfer of plasma contents between RE zone and untreated tissues. This further confirm a lack of severe damage to liver vascular structure in the RE zone after IRE. This preserved blood flow and efflux in the RE zone suggest that additionally delivered agents to the liver has the ability to penetrate tissue and ECM in the RE zone of the treated region, making the RE zone a target for vascular delivery of adjuvant therapy after IRE for improvement of IRE treatment efficacy.

Our studies had several shortcomings. For one, we were unable to stain and measure multivessel density on histologic sections of the tissue as liver sinusoidal endothelial cells do not stain positively for the same classical vascular markers. Second, we did not use enough numbers of animals to achieve sufficient power for generating correlation between imaging measurements and histologic measurements. Lastly, this study was performed on normal liver tissue, and future studies will analyze tissue perfusion after IRE in liver tumors.

In conclusion, DCE-MRI and DWI parameters allow differentiation between RE and IRE zones in a rabbit liver model.

Acknowledgements

We would like to acknowledge Matteo Figini for his assistance with MRI imaging and funding from the National Institute of Health. This study was supported by the National Cancer Institute (grants R01CA209886, R01CA196967), by 2019 Harold E. Eisenberg Foundation Scholar Award and by the Fishel Fellowship Award at the Robert H. Lurie Comprehensive Cancer Center.

Disclosure of conflict of interest

None.

Address correspondence to: Zhuoli Zhang, Department of Radiology, Feinberg School of Medicine, Northwestern University, Chicago, IL, USA. E-mail: zhuoli-zhang@northwestern.edu

References

[1] Rubinsky B, Onik G and Mikus P. Irreversible electroporation: a new ablation modality--clinical implications. Technol Cancer Res Treat 2007; 6: 37-48.

[2] Lee EW, Chen C, Prieto VE, Dry SM, Loh CT and Kee ST. Advanced hepatic ablation technique for creating complete cell death: irreversible electroporation. Radiology 2010; 255: 426-433.

[3] Daniels C and Rubinsky B. Electrical field and temperature model of nonthermal irreversible electroporation in heterogeneous tissues. J Biomech Eng 2009; 131: 071006.

[4] Silk M, Tahour D, Srimathveeravalli G, Solomon SB and Thornton RH. The state of irreversible electroporation in interventional oncology. Semin Intervent Radiol 2014; 31: 111-117.

[5] Guo Y, Zhang Y, Nijm GM, Sahakian AV, Yang GY, Omary RA and Larson AC. Irreversible electroporation in the liver: contrast-enhanced inversion-recovery MR imaging approaches to differentiate reversibly electroporated penumbra from irreversibly electroporated ablation zones. Radiology 2011; 258: 461-468.

[6] Niessen C, Thumann S, Beyer L, Pregler B, Kramer J, Lang S, Teufel A, Jung EM, Stroszczynski C and Wiggermann P. Percutaneous irreversible electroporation: long-term survival analysis of 71 patients with inoperable malignant hepatic tumors. Sci Rep 2017; 7: 43687.

[7] Sanchez-Velazquez P, Castellvi Q, Villanueva A, Iglesias M, Quesada R, Panella C, Caceres M, Dorcaratto D, Andaluz A, Moll X, Burdio JM, Grande L, Ivorra A and Burdio F. Long-term effectiveness of irreversible electroporation in a murine model of colorectal liver metastasis. Sci Rep 2017; 7: 44821.

[8] Maor E, Ivorra A, Mitchell JJ and Rubinsky B. Vascular smooth muscle cells ablation with endovascular nonthermal irreversible electroporation. J Vasc Interv Radiol 2010; 21: 1708-1715.

[9] Zmuc J, Gasljevic G, Sersa G, Edhemovic I, Boc N, Seliskar A, Plavec T, Brloznik M, Milevoj N, Brecelj E, Kos B, Izlakar J, Jarm T, Snoj M, Stukelj M, Miklavcic D and Cemazar M. Large liver blood vessels and bile ducts are not damaged by electrochemotherapy with bleomycin in pigs. Sci Rep 2019; 9: 3649.

[10] Zhang Y, White SB, Nicolai JR, Zhang Z, West DL, Kim DH, Goodwin AL, Miller FH, Omary RA and Larson AC. Multimodality imaging to assess immediate response to irreversible electroporation in a rat liver tumor model. Radiology 2014; 271: 721-729.

[11] Zhang Y, Guo Y, Ragin AB, Lewandowski RJ, Yang GY, Nijm GM, Sahakian AV, Omary RA and Larson AC. MR imaging to assess immediate response to irreversible electroporation for targeted ablation of liver tissues: preclinical feasibility studies in a rodent model. Radiology 2010; 256: 424-432.

[12] Felker ER, Dregely I, Chung DJ, Sung K, Osuagwu FC, Lassman C, Sayre J, Wu H and Lu DS. Irreversible electroporation: defining the MRI appearance of the ablation zone with histopathologic correlation in a porcine liver model. AJR Am J Roentgenol 2017; 208: 1141-1146.

[13] Padia SA, Johnson GE, Yeung RS, Park JO, Hippe DS and Kogut MJ. Irreversible electroporation in patients with hepatocellular carcinoma: immediate versus delayed findings at MR imaging. Radiology 2016; 278: 285-294.

[14] Lee GK, Suh KJ, Kang IW, Hwang DH, Min SJ, Han YM and Choi MH. MR imaging findings of high-voltage electrical burns in the upper extremities: correlation with angiographic findings. Acta Radiol 2011; 52: 198-203.

[15] Padhani AR, Liu G, Koh DM, Chenevert TL, Thoeny HC, Takahara T, Dzik-Jurasz A, Ross BD, Van Cauteren M, Collins D, Hammoud DA, Rustin GJ, Taouli B and Choyke PL. Diffusion-weighted magnetic resonance imaging as a cancer biomarker: consensus and recommendations. Neoplasia 2009; 11: 102-125.

[16] Qin L, Li X, Stroiney A, Qu J, Helgager J, Reardon DA and Young GS. Advanced MRI assessment to predict benefit of anti-programmed cell death 1 protein immunotherapy response in patients with recurrent glioblastoma. Neuroradiology 2017; 59: 135-145.

[17] Nakamura Y, Bernardo M, Nagaya T, Sato K, Harada T, Choyke PL and Kobayashi H. MR imaging biomarkers for evaluating therapeutic effects shortly after near infrared photoimmunotherapy. Oncotarget 2016; 7: 17254-17264.

[18] Ceschin R, Kurland BF, Abberbock SR, Ellingson BM, Okada H, Jakacki RI, Pollack IF and Panigrahy A. Parametric response mapping of apparent diffusion coefficient as an imaging biomarker to distinguish pseudoprogression from true tumor progression in peptide-based vaccine therapy for pediatric diffuse intrinsic pontine glioma. AJNR Am J Neuroradiol 2015; 36: 2170-2176.

[19] Chen BB, Hsu CY, Yu CW, Liang PC, Hsu C, Hsu CH, Cheng AL and Shih TT. Early perfusion changes within 1 week of systemic treatment measured by dynamic contrast-enhanced MRI may predict survival in patients with advanced hepatocellular carcinoma. Eur Radiol 2017; 27: 3069-3079.

[20] Hectors SJ, Wagner M, Bane O, Besa C, Lewis S, Remark R, Chen N, Fiel MI, Zhu H, Gnjatic S, Merad M, Hoshida Y and Taouli B. Quantification of hepatocellular carcinoma heterogeneity with multiparametric magnetic resonance imaging. Sci Rep 2017; 7: 2452.

[21] Ahmed Z and Levesque IR. An extended reference region model for DCE-MRI that accounts for plasma volume. NMR Biomed 2018; 31: e3924.

[22] Heye T, Davenport MS, Horvath JJ, Feuerlein S, Breault SR, Bashir MR, Merkle EM and Boll DT. Reproducibility of dynamic contrast-enhanced MR imaging. Part I. Perfusion characteristics in the female pelvis by using multiple computer-aided diagnosis perfusion analysis solutions. Radiology 2013; 266: 801-811.

[23] Thandassery RB, Goenka U and Goenka MK. Role of local ablative therapy for hepatocellular carcinoma. J Clin Exp Hepatol 2014; 4: S104-111.

[24] Nemcek AA. Complications of radiofrequency ablation of neoplasms. Semin Intervent Radiol 2006; 23: 177-187.

[25] Rhim H. Complications of radiofrequency ablation in hepatocellular carcinoma. Abdom Imaging 2005; 30: 409-418.
[26] Hinshaw JL, Lubner MG, Ziemlewicz TJ, Lee FT Jr and Brace CL. Percutaneous tumor ablation tools: microwave, radiofrequency, or cryoablation--what should you use and why? Radiographics 2014; 34: 1344-1362.
[27] Fairchild AH, Tatli S, Dunne RM, Shyn PB, Tuncali K and Silverman SG. Percutaneous cryoablation of hepatic tumors adjacent to the gallbladder: assessment of safety and effectiveness. J Vasc Interv Radiol 2014; 25: 1449-1455.
[28] Daher S, Massarwa M, Benson AA and Khoury T. Current and future treatment of hepatocellular carcinoma: an updated comprehensive review. J Clin Transl Hepatol 2018; 6: 69-78.
[29] Tao X, Wang L, Hui Z, Liu L, Ye F, Song Y, Tang Y, Men Y, Lambrou T, Su Z, Xu X, Ouyang H and Wu N. DCE-MRI perfusion and permeability parameters as predictors of tumor response to CCRT in patients with locally advanced NSCLC. Sci Rep 2016; 6: 35569.
[30] Thng CH, Koh TS, Collins DJ and Koh DM. Perfusion magnetic resonance imaging of the liver. World J Gastroenterol 2010; 16: 1598-1609.
[31] Tofts PS, Brix G, Buckley DL, Evelhoch JL, Henderson E, Knopp MV, Larsson HB, Lee TY, Mayr NA, Parker GJ, Port RE, Taylor J and Weisskoff RM. Estimating kinetic parameters from dynamic contrast-enhanced T(1)-weighted MRI of a diffusable tracer: standardized quantities and symbols. J Magn Reson Imaging 1999; 10: 223-232.
[32] Yang JF, Zhao ZH, Zhang Y, Zhao L, Yang LM, Zhang MM, Wang BY, Wang T and Lu BC. Dual-input two-compartment pharmacokinetic model of dynamic contrast-enhanced magnetic resonance imaging in hepatocellular carcinoma. World J Gastroenterol 2016; 22: 3652-3662.
[33] Chen BB and Shih TT. DCE-MRI in hepatocellular carcinoma-clinical and therapeutic image biomarker. World J Gastroenterol 2014; 20: 3125-3134.